

Article

A Computational Geometric Parameter Optimization of the Thermomechanical Deicing Concept

Ozan Tamer , Fabian Walter , Michael Sinapius *  and Markus Böl 

Institute of Mechanics and Adaptronics, Langer Kamp 6, Technical University of Braunschweig, 38106 Braunschweig, Germany

* Correspondence: m.sinapius@tu-braunschweig.de

Abstract: Ice formation on aerodynamic surfaces is a safety-related issue in aviation. Thermal, mechanical, or hybrid systems are used to prevent or eliminate ice formation. To increase energy efficiency, new methods are being researched and tested, using new materials. This article aims to investigate in detail the geometrical parameters of a novel thermomechanical deicing concept based on the shape memory effect. The thermomechanical behavior of a shape memory alloy wire embedded in an elastomer can be described, using the transformation expansion coefficient. The approach includes the nonlinear phase transformation and the linear expansion of the alloy. Simulation results using the above approach are compared with experimental results. In addition, a parameter study of the geometric quantities is presented, where the individual effects of these quantities are investigated assuming that there is a block-like ice layer on the surface. The results for the behavior of the SMA show promising results in terms of describing the thermomechanical behavior of the wire. However, deviations are still observed in the thermal behavior of the embedding matrix.

Keywords: shape memory alloys ; thermomechanical model; deicing concept



Citation: Tamer, O.; Walter, F.; Sinapius, M.; Böl, M. A Computational Geometric Parameter Optimization of the Thermomechanical Deicing Concept. *Actuators* **2022**, *11*, 223. <https://doi.org/10.3390/act11080223>

Academic Editor: Hongli Ji

Received: 29 June 2022

Accepted: 3 August 2022

Published: 5 August 2022

Publisher's Note: MDPI stays neutral with regard to jurisdictional claims in published maps and institutional affiliations.



Copyright: © 2022 by the authors. Licensee MDPI, Basel, Switzerland. This article is an open access article distributed under the terms and conditions of the Creative Commons Attribution (CC BY) license (<https://creativecommons.org/licenses/by/4.0/>).

1. Introduction

Shape memory alloy (SMA) materials are classified as active functional materials that convert energy [1]. Due to their reversible diffusionless phase transformation, they can change the microstructure upon thermal or mechanical impact. SMAs are characterized by a high energy density ($\approx 10 \text{ MJ m}^{-3}$) and large active strains of up to 7% compared to other smart materials [2]. In contrast, the higher the strain level, the fewer cycles of contraction–elongation will be repeated [3].

As a result of its shape memory effect, pseudoelastic behavior, and biocompatibility, the material has a wide range of potential applications, including aerospace (variable geometry chevron [4]) and medical applications (Nitinol braces for dental usage, cardiovascular devices, etc. [2]).

Pseudoelasticity, shape memory effect, and phase transformation are among the well-known phenomena of the SMA. Though these phenomena occur primarily at the microscopic level, they affect the macroscopic behavior of the SMA through thermal or mechanical effects that manifest themselves as shape recovery or deformation [5]. In order to describe the thermomechanical behavior of SMAs, modeling is performed according to microscopic (metallurgical properties) or macroscopic (phenomenological properties) aspects. In addition, there is also a mesoscopic approach, which deals with the lattice of the particles [5]. Close-to-reality modeling allows better predicting the nonlinear and hysteretic behavior of the material in the application. Different modeling approaches have been proposed for the prediction of such material behavior. The modeling of the SMA itself, however, has become an extensive topic in the literature. For this reason, a brief look at these references is mentioned here.

Paiva and Savi's research [6] includes a review on constitutive models (polynomial model, phase transformation kinetics and the model with internal constraints) in terms

of their mathematical description. Lagoudas [2] provided a chronological summary of commonly used constitutive SMA models for 1D (1986–2005) and 3D (1987–2008) and their characteristics. Patoor et al. [7] concentrated in their work on modeling at the single-crystal level. Lagoudas et al. [8] report modeling results for a polycrystalline SMA in their work, taking into account micromechanical and phenomenological methods. Khandelwal and Buravalla [9] classified the models as microscopic and macroscopic approximations.

In this study, we focus on phenomenological modeling concepts as numerous studies have taken a phenomenological approach. In this aspect, Tanaka [10] used an exponential strain hardening approach to describe the relationship between the martensite fraction (ζ) and temperature (T). Liang and Rogers [11], on the other hand, preferred the cosine function as the hardening function to describe the ζ – T relationship for their one-dimensional model. The internal variable of the martensite fraction was divided into a temperature-related and a stress-related component by Brinson [12]. This type of derivation allowed the representation of pseudoelastic and shape memory effects. Tagaki et al. [13] proposed a phenomenological approach for simulating hysteric a two-way shape memory effect (TWSME) by an equivalent thermal expansion coefficient for SMA plates.

1.1. A Brief Look into Deicing Systems

The conventional approach to remove ice from aerodynamic surfaces includes pneumatic deicing boots (mechanical deicing), hot bleed air (thermal anti-icing/deicing), and glycol-based fluid (chemical deicing) [14].

In conjunction with lightweight materials and a more energy-efficient trend, alternative anti-icing systems are required. Since this work is focused on thermomechanical deicing concepts, this part reviews the literature regarding alternative deicing systems, using an SMA for the aerospace industry. The study by Gerardi et al. [15] on SMA-based deicing systems was among the earliest. In their paper, SMA actuators were used to deice the leading edge of a rotor blade. An investigation is conducted in this paper to evaluate active (activating the SMA by heating) and passive (activating the SMA by latent heat from ice) deicing systems. By embedding Nitinol wires in the semicircular cylindrical shell, Myose et al. [16] constructed a functional composite material. This shape is meant to roughly simulate an aircraft wing's leading edge. A prototype leading edge was developed by Sullivan et al. [17] using thin aluminum sheets and SMA wires. The design parameters such as wire diameter, number of SMA wires, and aluminum sheet thickness are determined using finite element analysis (FEA). Activation of the wires causes a change in the shape of the aluminum surface. A deicer based on an SMA sheet was designed and numerically examined by Liu et al. [18]. The study aims to evaluate the deicing performance of an SMA deicer on fixed-wing structures and engines. A thermomechanical deicing concept using an SMA was previously proposed by Tamer et al. [19]. As a result of Joule heating, an SMA embedded in elastomer causes its temperature to increase, which triggers the activation of the SMA and its contraction. As a result of these thermal and mechanical effects, the matrix temperature increases and the surface changes. Based on the experimental findings, the functional specimen operated as a single heat-driven deicing system due to the dominant thermal effect.

1.2. Thermomechanical Deicing Concept Using an SMA Actor

The basic idea of the thermomechanical deicing concept underlying this article is to couple mechanical shear stresses with thermal heat fluxes to reduce the ice adhesion strength of an ice layer on a flowed surface, resulting in coupled mechanical and thermal deicing. For this purpose, a ring-shaped actuator made of a NiTi shape memory alloy (SMA) is embedded in an elastomer matrix. The electrical wire and thermocouple are connected to the SMA wire by crimping (Figure A2). Although the electrical wires and the thermocouple in the elastomer are additional materials that were not considered in the simulation, their influence on the deformation is negligible [20]. Joule heating due to current flow through the SMA wire in the circular actuator leads to initial phase transformation. Consequently,

the elastomer matrix converts the deformation and generated heat of the actuator into shear stress and heat of fusion at the surface, which in turn reduces the adhesive forces of the ice layer. Once the wire stops generating heat, the elastomer should restore the SMA ring's original position [19]. The extrinsic TWSME is initiated by the mutual work of the elastomer spring force and the ring. However, further experiments have shown that the elastomer surface does not completely recover after each additional cycle [20]. The coupled use of the various deicing functions within this hybrid principle is illustrated in Figure 1. The concept is expected to achieve higher efficiency compared to existing state-of-the-art deicing concepts. The reason is that SMA behaves like a natural hybrid system (thermo-mechanical) in this situation. In the functional sample, it is not only the mechanical deformation that is used, but also the thermal effect to weaken the ice adhesion.

Efficient system operation requires maximum functional conformity between the embedded actuator and the matrix. Functional conformity refers to the harmonization of competing and noncompeting target parameters of all features of an adaptive structure [1]. For optimal system behavior, the geometric and material parameters must be carefully matched. For this purpose, a parametric finite element (FE) model of the deicing concept is used, which also includes a nonlinear material model of the SMA actuator. To describe the deformation of the TWSME due to phase transformations, this work follows a phenomenological approach using an equivalent temperature-dependent thermal expansion transformation function.

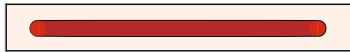
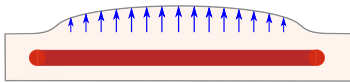
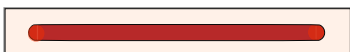
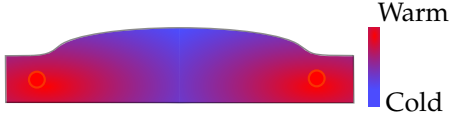
Effect	Initial State	SMA activated
Mechanical		
Thermal		

Figure 1. Representation of the effect with SMA activation [19].

The main objective of the described work is to geometrically optimize the existing concept. To this end, finite element method (FEM) parameter studies provide the resulting shear stresses, deformations, and temperatures at the surface of the deicing concept to provide improved conceptual parameters. In this context, an FE model of the concept, including the use of a phenomenological TWSME material model, will be created.

2. Materials and Methods

The FE model aims to describe the thermally and mechanically coupled nonlinear deformation of the shape memory alloy ring actuator and the hyperelastic material behavior of the matrix (Table A1).

2.1. Shape Memory Alloy Material Model

The consequence of the thermal activation of shape memory alloys is strong shape changes due to microstructural transformations between the martensitic to austenitic phase, which is called the TWSME. Actuator utilization of the TWSME is achieved by thermal cycling along a specific loading path, which constitutes thermomechanical training [2]. After each cycle of thermomechanical training, some plastic strain remains, which gradually saturates at about 100 cycles. This is due to unrecoverable defects in the microstructure of the SMA, which lead to an accumulation of oriented martensite and, thus, to an internal stress state [2,21]. While common material models describe this transformation behavior based on a Helmholtz free energy formulation, our modeling approach takes a phenomenological approach. Here, the inelastic deformation caused by a microstructural

transformation is represented by an equivalent thermal expansion. The total increase of inelastic strains $d\epsilon_{IE}$, according to Equation (1), consists of the linear thermal expansion component $d\epsilon_T$ and the nonlinear transformation-induced component $d\epsilon_{fwd,bwd}$ due to the TWSME. In this way, the transformation function, established by Tagaki et al. [13], represents the equivalent thermal expansion coefficient $\alpha_{fwd,bwd}$ according to Equation (2). In particular, the transformation behavior is determined by the transformation temperatures martensite start (M_s), austenite start (A_s), martensite finish (M_f), and austenite finish (A_f), the maximum transformation strain ϵ_{max} , the temperature T , and a slope control parameter K . The strain response in Figure 2 shows the ability of the existing TWSME model to map the large, nonlinear deformation, introduced by the TWSME. However, the stress dependence of the transformation temperatures is not represented by the existing model.

$$d\epsilon_{IE} = -\alpha_{fwd,bwd}dT + \alpha_T dT \quad (1)$$

$$\alpha_{fwd} = \frac{\epsilon_{max}}{2} \left[1 - \tanh^2 \left(K \frac{T - 0.5(A_s + A_f)}{0.5(A_f - A_s)} \right) \right] \frac{K}{0.5(A_f - A_s)} \quad (2)$$

$$\alpha_{bwd} = \frac{\epsilon_{max}}{2} \left[1 - \tanh^2 \left(K \frac{T - 0.5(M_s + M_f)}{0.5(M_s - M_f)} \right) \right] \frac{K}{0.5(M_s - M_f)}$$

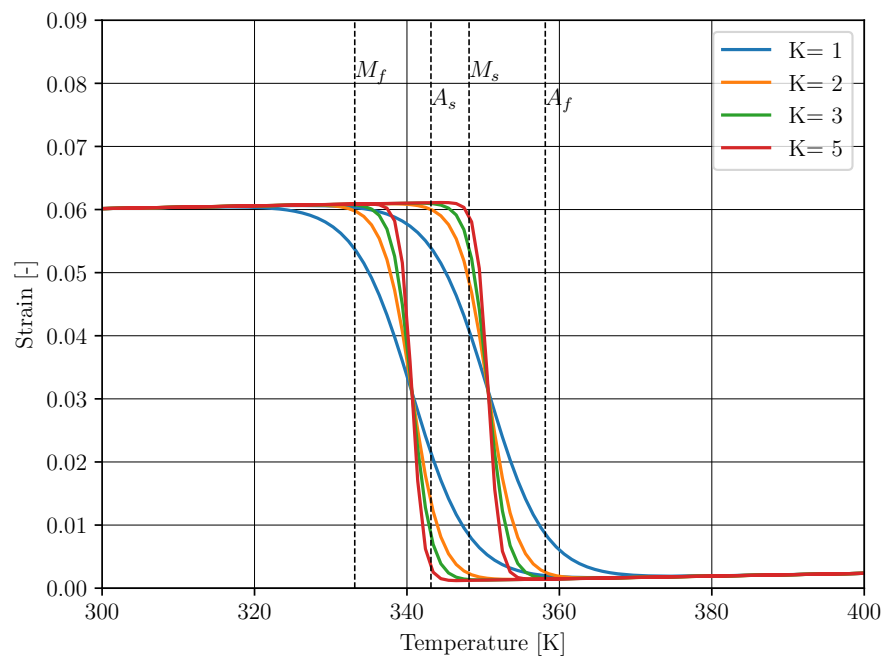


Figure 2. TWSME strain response as a function of temperature regarding different values of K .

2.2. FEM Model of the Deicing Concept

The geometrical structure and the main geometrical parameters, governing the thermal and mechanical performance of the hybrid deicing concept, are highlighted in Figure A1. The ring-shaped actuator has a wire loop diameter d_L and a wire diameter d_W , which is planar embedded with a defined distance to the symmetry plane of the matrix. The eccentric position of the wire is described by the relative eccentricity e , i.e., the ratio between the distance to the symmetry plane and the total distance between the symmetry plane and the top surface. The inscribed circle diameter of the segment determines the total width of the deicing system.

With regard to the mechanical boundary conditions, the rear wall of the system is rigidly supported, while the top and bottom sides are unconfined. Taking advantage of the symmetry of the deicing concept, the corresponding boundary conditions are introduced in the cross-sectional planes, following Figure A3. Hence, a one-twelfth segment satisfies to

represent the entire system. Furthermore, it can be assumed that the cross-sectional planes, the back wall plane, and the bottom plane behave adiabatically (Figure A3). In the initial state, the wire and matrix were assumed to be stress-free and have an ambient temperature of 298.15 K in all nodes.

The mechanical behavior of the isotropic nonlinear elastomer matrix is described by the Mooney–Rivlin strain energy potential, which is given in Equation (3). Due to the incompressibility of the elastomer material, $\lambda_1 \cdot \lambda_2 \cdot \lambda_3 = 1$ was considered. The invariants I_1 and I_2 of the right *Cauchy–Green* tensor can be assumed according to Equation (3). Since the deformation rates were assumed to be small, viscoelastic effects can be disregarded. The thermal behavior of the elastomer matrix was assumed to be sufficiently isotropic and linear. It follows that the quantities thermal conductivity k , specific heat capacity c_p , coefficient of thermal expansion α_T , and density ρ are uniformly distributed, constant, and assumed to be temperature independent. The material properties used are listed in Table A1. Since the thermal and mechanical fields are strongly coupled and large deformations occur, a fully coupled transient thermal stress analysis was performed for the deicing concept using ABAQUS®. In total, 26,711 cubic temperature displacement elements, resulting in 29,872 nodes, were used for the segment and for the ring actuator. To counteract volumetric locking, the elements of the incompressible elastomer matrix were considered in a hybrid, mixed formulation. When investigating the influence of the geometric parameters on the mechanical performance of the concept, thermal effects were initially neglected, i.e., a static mechanical analysis was performed. In order to investigate the influence of the parameters on the thermal system behavior, an uncoupled heat transfer analysis was carried out. The type of ice layer formed during icing depends in particular on the duration of icing, the liquid water content, and the flow velocity of the air. As a result, the accumulated ice layer exhibits a wide variety of mechanical and, in particular, adhesive properties. In general, a thick layer behaves rather rigidly and inhibits the heat flow to the surroundings, while a thin ice layer shows rather low rigidity and tends to dissipate heat to the surroundings. For simplification, the varying condition of accumulated ice is mapped by two edge cases in the deicing simulations. On the one hand, the edge case of a very thin ice layer, permitting heat conduction to the surrounding and an unconfined displacement of the segment, was considered. Here, we assumed a convection coefficient of $2.5 \text{ W K}^{-1} \text{ m}^{-2}$. In the aspect of a second edge case, an undetermined thick ice layer disables a displacement of the segment surface and heat transfer to the surroundings, represented by a confined and adiabatic top surface. In conclusion, the behavior of accumulated ice layers is adopted by the boundary conditions of the top surface.

$$\begin{aligned} W &= c_{10}(I_1 - 3) + c_{01}(I_2 - 3) + c_{11}(I_1 - 3)(I_2 - 3) \\ I_1 &= \lambda_1^2 + \lambda_2^2 + \lambda_3^2 \\ I_2 &= \lambda_2^2\lambda_3^2 + \lambda_1^2\lambda_3^2 + \lambda_1^2\lambda_2^2 \end{aligned} \quad (3)$$

3. Results

3.1. Model Validation

Figure 3 compares the deformation response of the thermomechanically coupled FE analysis with the measured displacement of a selected set of points from the published work of Tamer et al. [19] for model validation. With a maximum vertical displacement of $u = 10.1 \text{ mm}$ (z-direction) and a measured maximum vertical displacement of $u = 9.46 \text{ mm}$, the mechanical response agrees well with the measurement. In addition, Figure 4 (left) shows the center displacement as a function of wire temperature and, thus, the mechanical operation of the concept. As can be seen, the deformation of the elastomer segment starts at A_s , reaches the maximum at A_f , and continues to reshape between M_s and M_f . The graph on the right side of Figure 4 compares the measured and calculated maximum temperature of the surface (blue represents the simulation and magenta the experimental result) and the actuator (yellow represents the simulation and green the experimental result) as a function of time. According to the conceptual design of Tamer et al. [19], a constant current of 2.6 A

and voltage of 2.1 V are applied during the measurement and simulation. During the uninterrupted electrical actuation phase of 186 s, an increasing temperature of the actuator and the segment surface is observed. All along the recovery phase, the temperatures decrease exponentially. The calculated temperature of the wire agrees well with the measured temperature of the thermocouple. However, the maximum temperatures at the surface differ. The calculation underestimates the measured temperature by 7 °C. This is due to an inaccurate knowledge of the thermal limits and quantities. In particular, the thermal conductivity, the specific heat capacity, and the convection coefficient, which determine the heat flow to the environment, are uncertain parameters. In order to be able to meet the thermal behavior more precisely, these parameters would have to be determined experimentally.

In addition, the model contains further simplifications regarding the mechanical behavior of the system. Consequently, it can be expected that the inelastic TWSME response is decisively larger when static stresses due to prestressing occurring. However, by adapting the maximum transformation strain to $\epsilon_{max} = 0.06$ with respect to the experimental results, the present model adopts both the intrinsic, thermally trained and the extrinsic, stress-dependent part of the TWSME. This can be concluded, since the maximum displacement shown in Figure 3 agrees well with the measurement. Consequently, the introduced prestress due to the manufacturing and the rising static stress during the contraction phase can be sufficiently mapped by the present model. On the other hand, in contrast to physical models, the tuning parameters ϵ_{max} and K need to be adapted to each individual physical problem again.

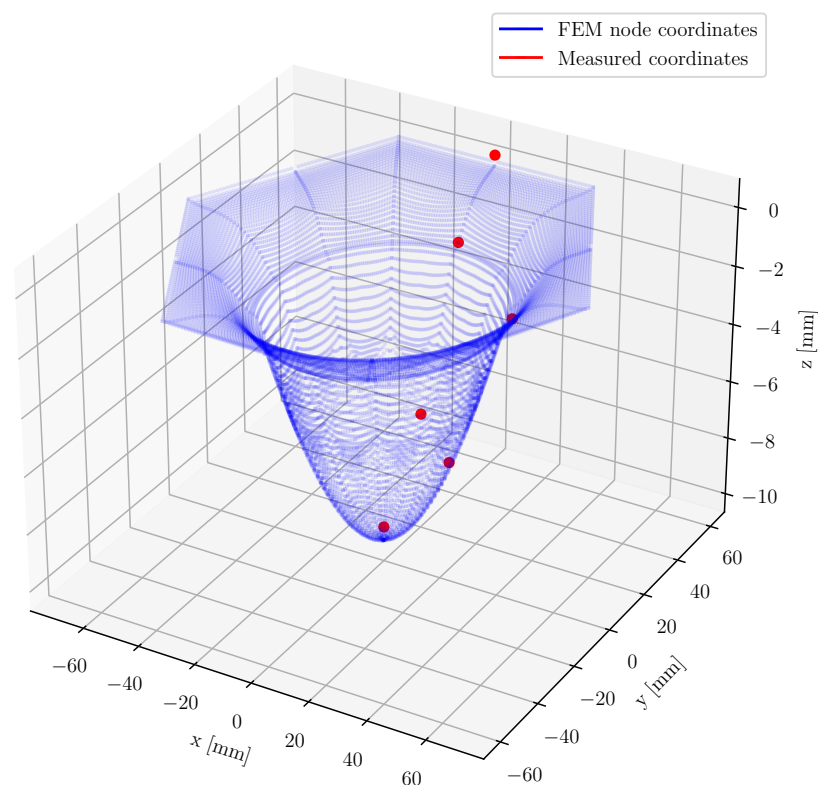


Figure 3. Comparison of the computed node displacement and the measured displacement at selected points of the concept with respect to Tamer et al. [19].

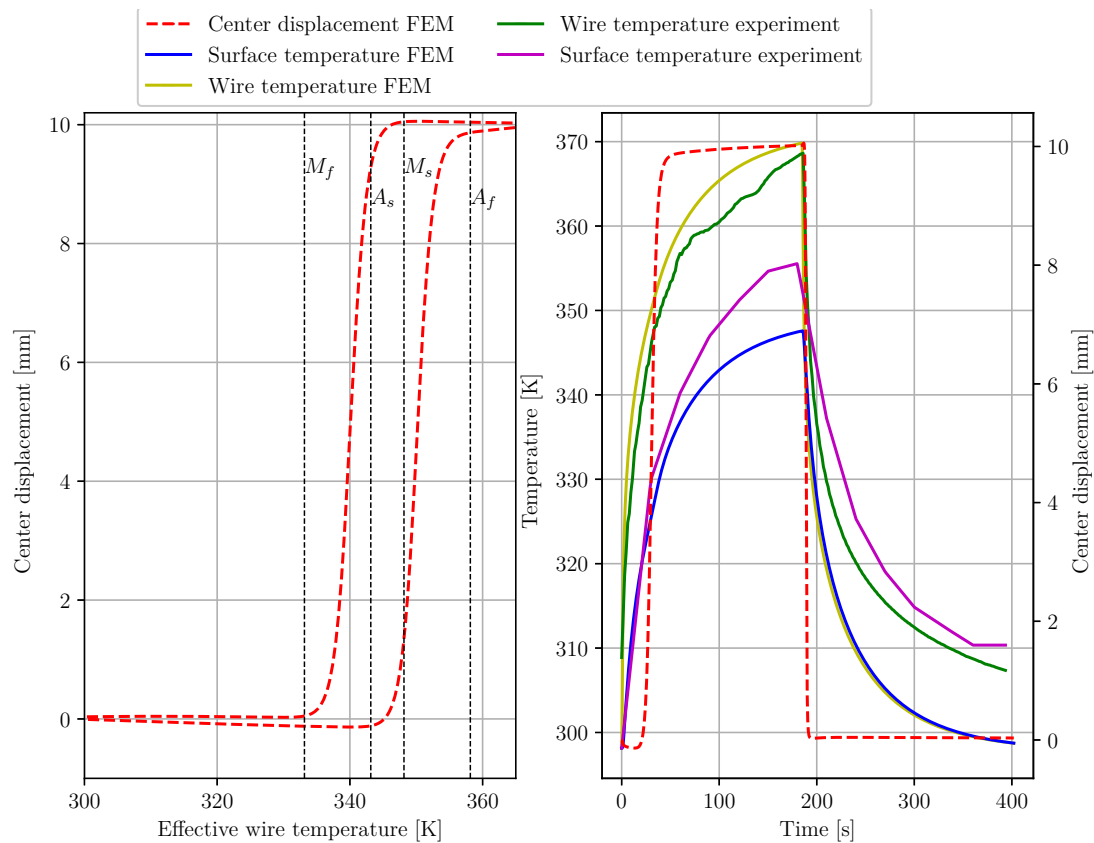


Figure 4. Comparison of the experimental and simulation results without an ice layer on the matrix surface.

3.2. Parameter Study

The variation of the governing geometrical parameters of the segment thickness h , relative eccentricity e , the wire loop diameter d_L , and the inscribed circle diameter d_h shows their influence on the thermal and mechanical performance. The range of the varied quantities is given with the minimum and maximum values in Table 1. A static mechanical analysis with respect to the described limit cases shows the resulting shear stress on the segment when a thick ice layer is considered, as well as the maximum displacement of the segment center concerning an almost infinitely thin layer.

The horizontal axes of the figures in this subsection have a scale from 0 to 1 or the lowest and the highest values of the varied quantity. In this way, the influence of the maximum and minimum values on the stresses and displacements is simulated. The highest values of the above parameters are given in Table 1.

Table 1. Maximum values for the relative magnitudes on the x-axis.

Parameter	Min. Value	Max. Value (100%)
Segment thickness (h)	2.47 mm	11 mm
Relative eccentricity (e)	−0.5	0.58
Wire loop diameter (d_{Lmax})	20 mm	90 mm
Inscribed circle diameter (d_h)	100 mm	200 mm

In the simulations, a very thick and an extremely thin ice layer on the surface of the matrix are defined as edge cases, as mentioned above. By a thick ice layer is meant a rigid adiabatic layer. This means that the matrix surface is completely confined. By a thin ice layer, reference is made to the free surface. Consequently, the surface is free from

mechanical constraints and natural convection heat transfer is possible. This allowed the ambient temperature to be assumed to be 25 °C in the simulations.

Figure 5 (left) shows the changes in the displacement of the center point by varying the relative magnitude of the four parameters in the case of a thick layer of ice on the matrix surface. Increasing the segment thickness while keeping the other parameters constant results in the segment becoming very stiff and almost impossible to bend under wire contraction. With regard to the inner circle diameter, no significant influence can be detected compared to other parameters. If we consider the hexagonal shape as a circular plate, we can better interpret the influence of the inner circle diameter. As Figure A4 shows, the radius of the circular plate is inversely proportional to the spring stiffness of the plate. The larger the diameter, the softer the plate becomes, making the structure easier to deform. According to Figure 5, the center displacement shows an upward trend as the diameter of the wire loop increases. This is an expected result because the longer the wire, the more it contracts and the matrix is forced into greater deflection. Figure 5 (right) illustrates the change of the maximum Mises stress of the interface between the segment and a thick ice layer over the changing geometrical parameters. Here, the infinitely thick, rigid ice layer constitutes an edge case, confining the whole segment surface. The increase of the segment thickness leads to a strong decrease of the stress, while the increase of the other values does not lead to a significant difference. The limited deformation on the surface due to the blocky ice and the insufficient contraction force of the wire also limit the stress generation.

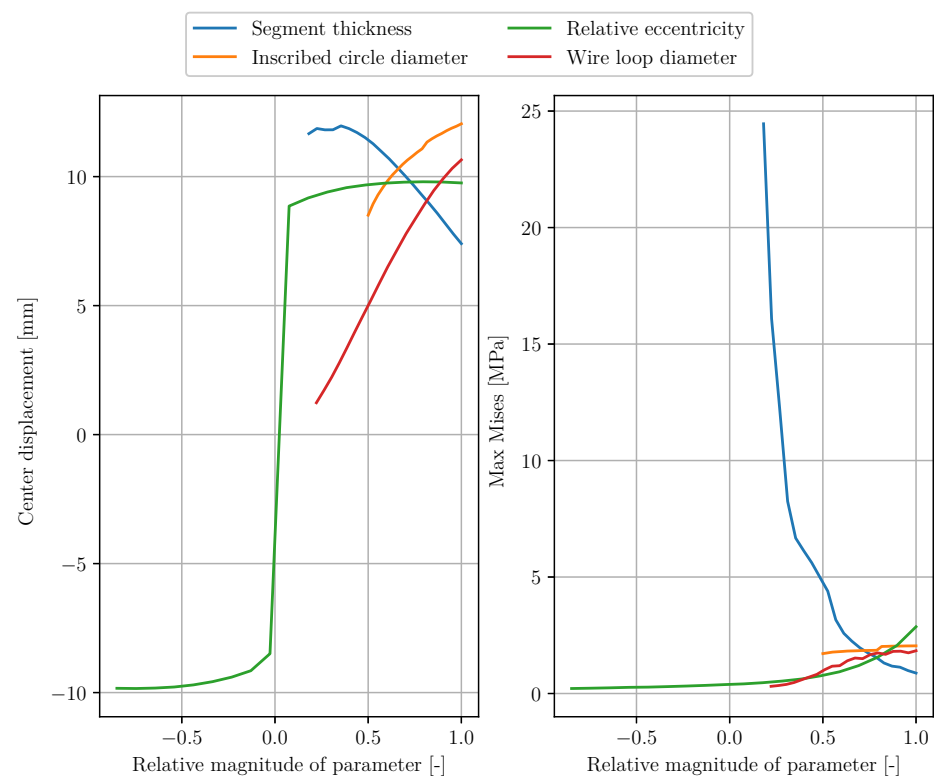


Figure 5. Max Mises vs. relative magnitude of all parameters in case of a thick ice layer on the matrix surface.

Figure 6 illustrates the maximum temperature on the surface as a result of the change in relative parameter size in the limiting case of a thin layer of ice on the matrix surface. Increasing the wire loop diameter moves the heat source to the edge of the structure. Assuming the solid surface to be adiabatic (Figure A3), in addition to the low thermal conductivity of the matrix material, causes the observed maximum temperature at the surface to decrease. Similarly, as the segment thickness increases, under the condition of 50% eccentricity, the distance between the surface and the heat source increases. As a

result, the maximum temperature at the surface decreases. On the other hand, the surface temperature can be obviously higher by increasing the relative eccentricity while keeping the segment thickness constant. In addition to the adiabatic assumption for the back side of the elastomer, the low thermal conductivity of the material also adds to the problem. Consequently, the outer side of the matrix behaves like a thermal insulation layer at higher inscribed diameters regardless of the assumption. For this reason, this parameter has a negligible influence on the maximum surface temperature.

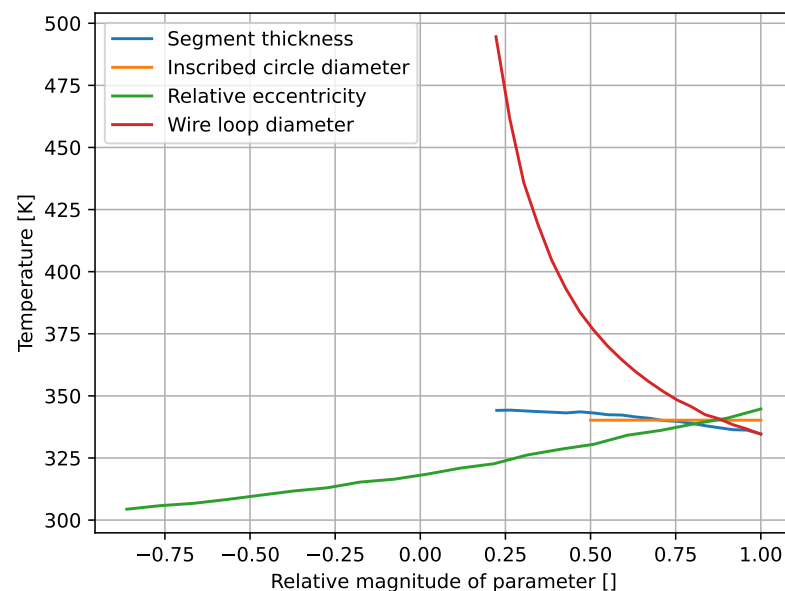


Figure 6. Maximum temperature vs. relative magnitude of all parameters in the case of a thin ice layer on the matrix surface.

4. Discussion

The transformation expansion coefficient approach to model the material behavior of the SMA provides promising results in terms of describing the thermomechanical behavior of the wire. The difference between the results for the matrix temperature values can be attributed to the measurement method used. To measure the wire temperature, a type K thermocouple was used with a metal sleeve that firmly connects the thermocouple to the wire. In addition, the temperature value on the surface was determined using a thermal imaging camera with a moving spotmeter, which is always the hottest temperature in the measurement range. The spotmeter does not measure a fixed point like the thermocouple.

In the remaining simulations, one parameter was defined as a variable in each calculation. Thus, the individual influences of the geometric variables could be studied. One of the limitations of the present studies is, of course, that the thermal behavior and the reaction of the ice layer were not taken into account because of the temperature rise at the interface.

For the mechanical effect to work, the ice layer must be intact and in contact with the surface. If the ice layer melts completely, the mechanical force cannot be transmitted.

During the assembly of the wire and the matrix, a pre-strain was added to the wire, leading to a stronger displacement due to the shape memory effect. The material formulation does not physically consider the stress dependency of the shape memory effect, but adopts this behavior phenomenologically, since we validated the formulation regarding the functional concept.

Another limitation of the present study naturally occurs due to the assembly of the wire with the desired preload. In the simulation, it was considered, of course, that the mounting of the wire in the functional pattern was ideal. However, in the real implementation, the pretensioned wire without loose contact with the inner part of the die did not emerge as planned. Loose contact of the wire means that the spring force of the matrix material cannot be transferred to the wire during the forward phase transformation. As a result, there is no

way to restore the shape of the surface. Since we are dealing with a single functional sample, it is not possible to investigate the variability of this specific case diversely. Moreover, the assembly was not performed by a standardized method. Therefore, the problem is a question related to experimental behavior.

Author Contributions: Writing—original draft preparation, O.T.; writing—review, software and visualization O.T. and F.W.; supervision, M.S. and M.B.; Funding acquisition O.T., M.S. and M.B. All authors have read and agreed to the published version of the manuscript.

Funding: This research was funded by Deutsche Forschungsgemeinschaft (DFG) Grant Number 456102901.

Institutional Review Board Statement: Not applicable.

Informed Consent Statement: Not applicable.

Data Availability Statement: All needed data for reproduction of results are contained within the article. The data presented in this study can be reproduced by given assumptions and equations.

Conflicts of Interest: The authors declare no conflict of interest.

Abbreviations

The following abbreviations are used in this manuscript:

bwd	backward
fwd	forward
FE	finite element
FEA	finite element analysis
FEM	finite element method
SMA	shape memory alloy
SME	shape memory effect
T	temperature
TWSME	two-way shape memory effect
α_{bwd}	coefficient of thermal expansion of the backward transformation
α_{fwd}	coefficient of thermal expansion of the forward transformation
α_T	coefficient of thermal expansion
c	spring constant
c_{ij}	material parameter for elastomer
c_p	specific heat capacity
d_h	inscribed circle diameter
d_L	wire loop diameter
d_w	wire diameter
e	relative eccentricity
ϵ	strain
ϵ_{IE}	inelastic strain
ϵ_{max}	maximum strain
E	elastic modulus
$E_{Austenit}$	elastic modulus (austenite)
G	shear modulus
h	segment thickness
$I_{1,2}$	invariants of the right Cauchy–Green tensor
k	thermal conductivity
K	constant for demonstrate of hysteresis behavior
$\lambda_{1,2,3}$	stretching in directions 1, 2 and 3
μ	Poisson's ratio
N	plate bending stiffness
R	plate radius
ρ	density
t	plate thickness
ζ	martensite fraction

Appendix A

Supplementary information to this article including geometric specifications, material properties (wire and matrix), and simulation data can be found in this section.

Appendix A.1. Figures Relating to Geometric Specifications

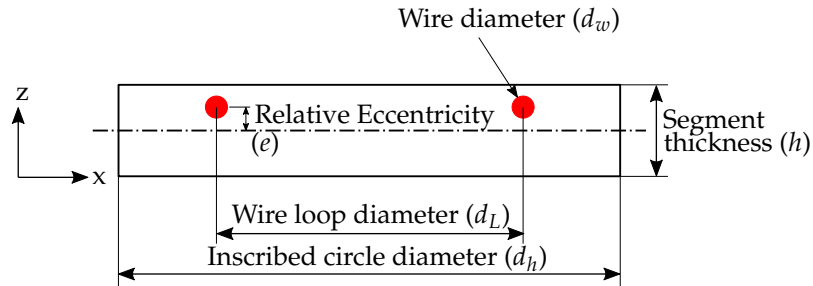


Figure A1. Geometric parameters from the cross-sectional view of the functional sample [19].

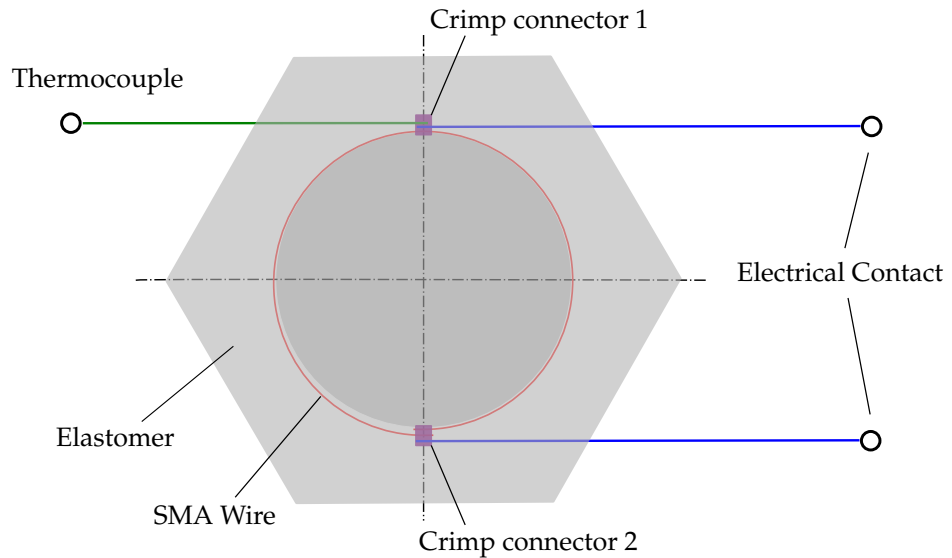


Figure A2. Cross-section presentation for electrical wire and thermocouple connection to the SMA wire, with the change from [19].

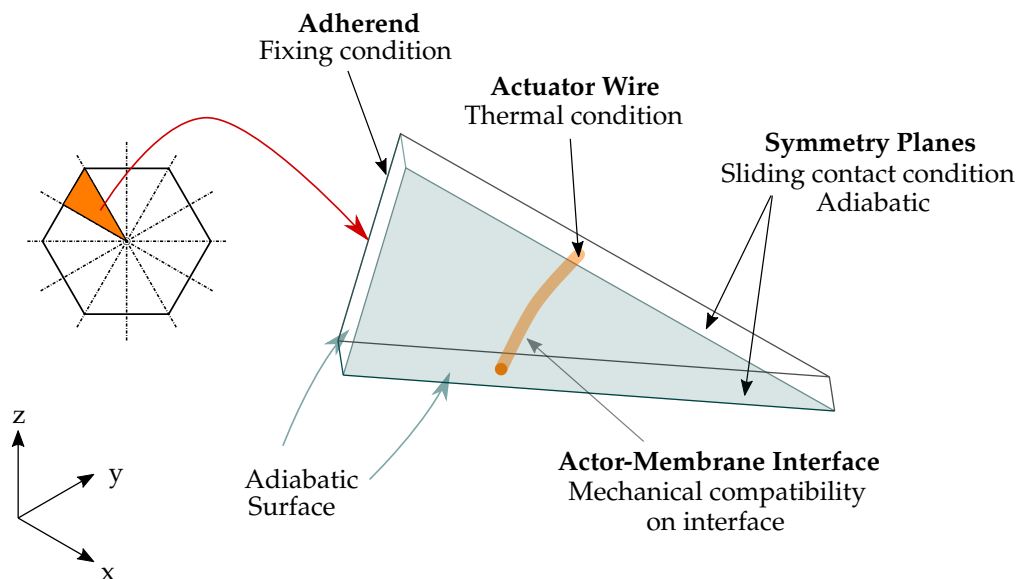


Figure A3. One-twelfth model and conditions for representing the symmetry and external mount [19].

Appendix A.2. Geometry and Material Properties of Matrix and SMA Wire

Table A1. Table of parameters for the geometry, matrix, and wire.

Parameter	Geometry	Matrix ¹	Wire
Segment thickness (h)	8 mm		
Relative eccentricity (e)	50%		
Wire loop diameter (d_L)	80 mm		
Wire diameter (d_w)	375 μm		
Inscribed circle diameter (d_h)	120 mm		
1/12 Segment angle	30°		
c_{01}		0.66 MPa	
c_{10}		−0.36 MPa	
c_{11}		0.24 MPa	
c_{02}		0 MPa	
c_{20}		0 MPa	
Thermal conductivity (k)		0.22 W m ^{−1} K	
Specific heat capacity (c_p)		1400 J kg ^{−1} K ^{−1}	
Density (ρ)		500 kg m ^{−3}	
Thermal expansion coefficient (α_T)		31 × 10 ^{−5} K ^{−1}	
α_T			22 × 10 ^{−5} K ^{−1}
$E_{Austenite} = E_{Martensite}$			70 GPa
Poisson's ratio			0.33
Thermal conductivity (k)			21 W m ^{−1} K ^{−1}
Specific heat capacity (c_p)			320 J kg ^{−1} K ^{−1}
Density (ρ)			6690 kg m ^{−3}
M_f			333.15 K
M_s			348.15 K
A_s			343.15 K
A_f			358.15 K

¹ Polynomial order hyperelastic material = 2.

Appendix A.3. Circular Plate Geometric Properties

Geometry	Geometric parameters	Spring constant
Circular plate, fixed at the circumference, central load.	Plate radius R Plate thickness t Plate stiffness N $N = \frac{Et^3}{12(1-\mu^2)} = \frac{Gt^3}{6(1-\mu)}$	 $c = \frac{16\pi N}{R^2}$

Figure A4. Geometric properties of circular plate [22].

Appendix A.4. Simulation Data

Table A2. Step and load data of the simulation.

Parameter	Value
Ambient temperature	298.15 K
Film coefficient convection	2.5 W m ^{−2} K ^{−1}
Time period actuation	402 s
t_{start} actuation	0 s
t_{step} actuation	200 s
t_{end} actuation	402 s

Table A2. Cont.

Parameter	Value
Initial increment actuation	0.5
Min. increment actuation	1×10^{-7}
Max. increment actuation	0.5
Max. number of increments	1×10^6
Current	2.6 C s^{-1}
Voltage	$2.1 \times 10^3 \text{ mJ C}^{-1}$

References

1. Sinapius, J.M. *Adaptronics-Smart Structures and Materials*; Springer: Berlin, Germany, 2021.
2. Lagoudas, D.C. *Shape Memory Alloys: Modeling and Engineering Applications*; Springer Science & Business Media: New York, NY, USA, 2008.
3. Lecce, L.; Concilio A. *Shape Memory Alloy Engineering: For Aerospace, Structural and Biomedical Applications*; Elsevier: Oxford, UK, 2014.
4. Mabe, J.; Calkins, F.; Butler, G. Boeing's variable geometry chevron, morphing aerostructure for jet noise reduction. In Proceedings of the 47th AIAA/ASME/ASCE/AHS/ASC Structures, Structural Dynamics, and Materials Conference, Newport, RI, USA, 1–4 May 2006; p. 2142.
5. Savi, M.A.; Paiva, A.; Pacheco, P.M. Phenomenological modeling of shape memory alloy thermomechanical behavior. In Proceedings of the International Symposium on Solid Mechanics, São Paulo, Brazil, 3–7 January 2007; pp. 497–511.
6. Paiva, A.; Savi, M.A. An overview of constitutive models for shape memory alloys. *Math. Probl. Eng.* **2006**, *2006*, 56876. [[CrossRef](#)]
7. Patoor, E.; Lagoudas, D.C.; Popov, P.; Entchev, P.B.; Brinson, L.C.; Gao, X. Shape memory alloys, Part I: General properties and modeling of single crystals. *Mech. Mater.* **2006**, *38*, 391–429. [[CrossRef](#)]
8. Lagoudas, D.C.; Entchev, P.B.; Popov, P.; Patoor, E.; Brinson, L.C.; Gao, X. Shape memory alloys, Part II: Modeling of polycrystals. *Mech. Mater.* **2006**, *38*, 430–462. [[CrossRef](#)]
9. Lagoudas, D.C.; Entchev, P.B.; Popov, P.; Patoor, E.; Brinson, L.C.; Gao, X. Models for shape memory alloy behavior: An overview of modeling approaches. *Int. J. Solids Struct.* **2009**, *1*, 111–148.
10. Tanaka, K. A thermomechanical sketch of shape memory effect: One-dimensional tensile behavior. *Res. Mech.* **1986**, *18*, 251–263.
11. Liang, C.; Rogers, C.A. One-dimensional thermomechanical constitutive relations for shape memory materials. *J. Intell. Mater. Syst. Struct.* **1990**, *1*, 207–234. [[CrossRef](#)]
12. Brinson, L.C.A. One-dimensional constitutive behavior of shape memory alloys: Thermomechanical derivation with non-constant material functions and redefined martensite internal variable. *J. Intell. Mater. Syst. Struct.* **1993**, *4*, 229–242. [[CrossRef](#)]
13. Takagi, T.; Luo, Y.; Suzuki, S.; Matsumoto, M.; Tani, J. Modeling and numerical simulation on thermomechanical behavior of SMA plates with two-way shape memory effect. *J. Intell. Mater. Syst. Struct.* **2001**, *12*, 721–728. [[CrossRef](#)]
14. Goraj, Z. An overview of the deicing and anti-icing technologies with prospects for the future. In Proceedings of the 24th International Congress of the Aeronautical Sciences, Yokohama, Japan, 29 August–3 September 2004.
15. Gerardi, J.; Ingram, R.; Catarella, R. A shape memory alloy based de-icing system for aircraft. In Proceedings of the 33rd Aerospace Sciences Meeting and Exhibit, Reno, NV, USA, 9–12 January 1995.
16. Myose, R.Y.; Horn, W.J.; Hwang, Y.; Herrero, J.; Huynh, C.; Boudraa, T. *Application of Shape Memory Alloys for Leading Edge Deicing*; SAE International: Warrendale, PL, USA, 1999.
17. Sullivan, D.B.; Righi, F.; Hartl, D.J.; Rogers, J. Shape Memory Alloy Rotor Blade Deicing. In Proceedings of the 54th AIAA/ASME/ASCE/AHS/ASC Structures, Structural Dynamics, and Materials Conference, Boston, MA, USA, 8–11 April 2013; p. 1915.
18. Liu, X.; Xing, Y.; Zhao, L. Study of shape memory alloy de-icing device for nonrotating components of aircrafts. In Proceedings of the IOP Conference Series: Materials Science and Engineering, Xishuangbanna, Yunnan, China, 16–17 June 2018; p. 032106.
19. Tamer, O.; Kyriazis, A.; Sinapius, M. Parameter study and experimental analysis of a thermo-mechanical de-icing concept. *Smart Mater. Struct.* **2020**, *29*, 045021. [[CrossRef](#)]
20. Kyriazis, A. Parameterstudie und Experimentelle Überprüfung eines Integrierten Thermo-Mechanischen Enteisungssystems. Master's Thesis, Technical University of Braunschweig, Braunschweig, Germany, 2018.
21. Xu, L.; Solomou, A.; Baxevanis, T.; Lagoudas, D.C. Finite strain constitutive modeling for shape memory alloys considering transformation-induced plasticity and two-way shape memory effect. *Int. J. Solids Struct.* **2021**, *221*, 42–59. [[CrossRef](#)]
22. Den Hartog, J.P. *Mechanische Schwingungen*; Springer: Berlin/Heidelberg, Germany, 2013.